

Stellar velocity dispersion and initial mass function gradients in dissipationless galaxy mergers

Carlo Nipoti^{1*}, Carlo Cannarozzo^{1,2}, Francesco Calura², Alessandro Sonnenfeld³ and Tommaso Treu⁴

¹*Department of Physics and Astronomy, University of Bologna, via Gobetti 93/2, I-40129 Bologna, Italy*

²*INAF - Astrophysics and Space Science Observatory of Bologna, via Gobetti 93/3, I-40129, Bologna, Italy*

³*Leiden Observatory, Leiden University, Niels Bohrweg 2, 2333 CA Leiden, The Netherlands*

⁴*Department of Physics and Astronomy, University of California, Los Angeles, CA, 90095-1547, USA*

Accepted, September 11 2020

ABSTRACT

The stellar initial mass function (IMF) is believed to be non-universal among early-type galaxies (ETGs). Parameterizing the IMF with the so-called IMF mismatch parameter α_{IMF} , which is a measure of the stellar mass-to-light ratio of an ensemble of stars and thus of the ‘heaviness’ of its IMF, one finds that for ETGs α_e (i.e. α_{IMF} integrated within the effective radius R_e) increases with σ_e (the line-of-sight velocity dispersion σ_{los} integrated within R_e) and that, within the same ETG, α_{IMF} tends to decrease outwards. We study the effect of dissipationless (dry) mergers on the distribution of the IMF mismatch parameter α_{IMF} in ETGs using the results of binary major and minor merging simulations. We find that dry mergers tend to make the α_{IMF} profiles of ETGs shallower, but do not alter significantly the shape of the distributions in the spatially resolved $\sigma_{\text{los}}\alpha_{\text{IMF}}$ space. Individual galaxies undergoing dry mergers tend to decrease their α_e , due to erosion of α_{IMF} gradients and mixing with stellar populations with lighter IMF. Their σ_e can either decrease or increase, depending on the merging orbital parameters and mass ratio, but tends to decrease for cosmologically motivated merging histories. The α_e - σ_e relation can vary with redshift as a consequence of the evolution of individual ETGs: based on a simple dry-merging model, ETGs of given σ_e are expected to have higher α_e at higher redshift, unless the accreted satellites are so diffuse that they contribute negligibly to the inner stellar distribution of the merger remnant.

Key words: galaxies: elliptical and lenticular, cD – galaxies: evolution – galaxies: formation – galaxies: interactions – galaxies: kinematics and dynamics – stars: luminosity function, mass function

1 INTRODUCTION

There is growing evidence that the stellar initial mass function (IMF) is not universal. Not only do different galaxies have different stellar IMFs, but, at least in some cases, there are indications that the IMF is also different in different regions of the same galaxy (see e.g. Hopkins 2018; Smith 2020). When the single stars are not resolved in observations, we have access only to indirect information about the stellar IMF, such as, for instance, the so called IMF mismatch parameter¹

$$\alpha_{\text{IMF}} \equiv \frac{(M_{\star}/L)_{\text{true}}}{(M_{\star}/L)_{\text{ref}}}, \quad (1)$$

where $(M_{\star}/L)_{\text{true}}$ is the true stellar mass-to-light ratio of an ensemble of stars (in a given band) and $(M_{\star}/L)_{\text{ref}}$ is the stellar mass-to-light ratio (in the same band) that one would infer assuming a reference IMF, for instance the Salpeter (1955), the Kroupa (2001) or the Chabrier (2003) IMF (Treu et al. 2010). α_{IMF} is a quantity integrated over the stellar population, which, per se, does not contain information on the *shape* of the IMF. Broadly speaking, IMFs with high α_{IMF} are said to be ‘heavy’: a high value of α_{IMF} can be due to an overabundance of low-mass stars (bottom-heavy IMF), but also of high-mass stars (top-heavy IMF; Bastian et al. 2010).

When large samples of massive early-type galaxies (ETGs) are considered, an empirical correlation is found between the IMF and the central stellar velocity dispersion, in the sense that ETGs with higher velocity dispersion have, on average, heavier IMF (Treu et al. 2010; Cappellari et al. 2012; Conroy & van Dokkum 2012; Dutton et al. 2012; Tortora et al. 2013; Spiniello et al. 2014; Li et al. 2017; Rosani et al. 2018). For instance, for a sample of

* E-mail: carlo.nipoti@unibo.it

¹ In the literature the IMF mismatch parameter α_{IMF} is sometimes referred to as effective IMF, mass excess or excess stellar mass-to-light ratio.

present-day ETGs with $90 \text{ km s}^{-1} \lesssim \sigma_e \lesssim 270 \text{ km s}^{-1}$, taking as reference IMF the Salpeter IMF, [Posacki et al. \(2015\)](#) find

$$\log \alpha_e = (0.38 \pm 0.04) \log \left(\frac{\sigma_e}{200 \text{ km s}^{-1}} \right) + (-0.06 \pm 0.01), \quad (2)$$

with intrinsic scatter 0.12 dex in α_e at given σ_e , where the *effective IMF mismatch parameter* α_e is the IMF mismatch parameter measured within the effective radius R_e and the *effective velocity dispersion* σ_e is the central stellar velocity dispersion measured within R_e . It must be stressed that some individual galaxies are found to deviate substantially from this relation: in particular, there are cases of massive (high- σ_e) ETGs with light IMF ([Smith et al. 2015](#); [Collier et al. 2018](#); [Sonnenfeld et al. 2019](#)).

Spatially resolved estimates of α_{IMF} in ETGs have revealed the presence of IMF gradients: α_{IMF} is higher in the centre than in the outer regions of individual galaxies, ranging from an IMF heavier than the Salpeter IMF to a lighter IMF with Chabrier-like α_{IMF} ([Martín-Navarro et al. 2015a](#); [Davis & McDermid 2017](#); [van Dokkum et al. 2017](#); [Zieleniewski et al. 2017](#); [Oldham & Auger 2018](#); [Sonnenfeld et al. 2018](#); [La Barbera et al. 2019](#); but see also [Alton et al. 2017, 2018](#) and [Vaughan et al. 2018](#), who find no significant IMF radial gradients in their samples of ETGs).

In the currently favoured hierarchical model of galaxy formation, ETGs are believed to form in two phases ([Oser et al. 2010](#)): a first mostly dissipative phase of in-situ star formation at $z \gtrsim 2$ and a second phase of accretion of stars mainly via dissipationless (‘dry’) mergers at $z \lesssim 2$ (see also section 10.8 of [Cimatti, Fraternali & Nipoti 2019](#)). In this context, the correlation between α_e and σ_e observed for present-day massive ETGs must be produced by the combination of the above two phases. Focusing on the second phase, [Sonnenfeld, Nipoti & Treu \(2017\)](#) studied the redshift evolution of the α_e - σ_e relation since $z \approx 2$, considering cosmologically motivated merging hierarchies in the simple case in which all the mergers are dissipationless and the stellar populations mix completely in the mergers. [Sonnenfeld et al. \(2017\)](#) found that, as a consequence of the accretion of lower-mass satellites, both σ_e and α_e of massive ETGs decrease with cosmic time. Nevertheless, in this model the α_e - σ_e relation remains essentially unaltered as cosmic time goes on, because individual massive ETGs move in the σ_e - α_e plane roughly along the α_e - σ_e relation.

The model of [Sonnenfeld et al. \(2017\)](#) is based on a few simplifying assumptions, which are only partially justified: the stellar velocity dispersion is assumed to be proportional to the host halo virial velocity dispersion, neither dissipation nor star formation is allowed during the merger, and any gradient in the α_{IMF} distribution within galaxies is neglected. [Blancato, Genel & Bryan \(2017\)](#) studied the same process with a more realistic, though not fully self-consistent approach, performing a post-processing analysis of the Illustris cosmological hydrodynamic simulation ([Vogelsberger et al. 2014](#)). [Blancato et al. \(2017\)](#) found that, at the time of star formation, α_{IMF} must vary strongly with the local velocity dispersion in order to reproduce the observed α_e - σ_e relation of present-day ETGs. More recently [Barber et al. \(2018, 2019a,b\)](#) revisited the problem of the theoretical origin and evolution of the α_e - σ_e relation of ETGs in a more self-consistent way by performing cosmological hydrodynamic simulations in which, when stars form, the IMF depends on the local pressure of the gas. The models considered by Barber et al., which are calibrated to reproduce the observed present-day trend of α_e increasing with σ_e , assume that in higher-pressure environments the stars form with heavier IMF, either bottom-heavy (model ‘LoM’) or top-heavy

(model ‘HiM’). [Barber et al. \(2019b\)](#) find that, at given σ_e , the average α_e of ETGs tends to be higher at higher z for model ‘LoM’, in which α_{IMF} is essentially independent of the age of the stellar population, and lower at higher z for model ‘HiM’, in which instead α_{IMF} is significantly lower for younger stellar populations. The question of the non-universality of the IMF in the context of galaxy formation and evolution has been explored also with semi-analytical models in various papers ([Nagashima et al. 2005](#); [Calura & Menci 2009](#); [Chattopadhyay et al. 2015](#); [Gargiulo et al. 2015](#); [Fontanot et al. 2017](#)), which however focus on the evolution of the chemical properties of galaxies without exploring specifically correlations of the IMF with the stellar velocity dispersion.

In this paper, we approach theoretically the question of the evolution of the α_{IMF} of ETGs by taking into account in detail α_{IMF} gradients within galaxies. In a cosmological context, the α_{IMF} gradients of simulated ETGs have been analyzed by both [Blancato et al. \(2017\)](#) and [Barber et al. \(2019b\)](#), who find that their simulated present-day ETGs have broadly realistic α_{IMF} profiles. In the case of [Barber et al. \(2019b\)](#), the α_{IMF} profiles tend to be steeper for model ‘LoM’ than for model ‘HiM’. Here we address the question of the evolution of the α_{IMF} gradients with a simpler approach, using binary dissipationless merging simulations, which are outside a fully cosmological framework. Though idealized in some respect, our simulations allow us to study in great detail the dynamical effects on the distribution of α_{IMF} , which are believed to be important in the second phase of ETG formation. With our approach, we can disentangle these dynamical effects from other effects more directly related to dissipation and star formation, which is not straightforward in cosmological hydrodynamic simulations.

If the IMF is not universal, the presence of IMF gradients within ETGs must be expected, because merging produces a partial mixing of the stellar populations ([White 1980](#)). For instance, in the idealized case of a binary dissipationless merger in which the two merging galaxies have different α_{IMF} and no α_{IMF} gradient, an α_{IMF} gradient will naturally arise in the remnant. More realistically, we can envisage an evolutionary scenario for ETGs in which galaxies with α_{IMF} gradients merge with other galaxies that have themselves α_{IMF} gradients and generally different average α_{IMF} . This is the approach we adopt in the models here presented.

The paper is organized as follows. The set-up and the analysis of the N -body simulations are described in Section 2 and Section 3, respectively. Our results are presented in Section 4. Section 5 concludes.

2 N-BODY SIMULATIONS

2.1 Sets of simulations

In this paper we analyze N -body simulations of binary dissipationless galaxy mergers presented in previous works. In particular, we focus on ten simulations taken from the simulation sets named D, D3 and D4 in [Sonnenfeld, Nipoti & Treu \(2014\)](#), some of which were originally presented in [Nipoti et al. \(2009\)](#) and [Nipoti et al. \(2012\)](#).

The six simulations of set D are characterized by different values of the stellar mass ratio $\xi_* = M_{*,\text{sat}}/M_{*,\text{main}}$ between the two progenitor galaxies: two with $\xi_* = 1$ (equal-mass major merger), two with $\xi_* = 0.5$ (unequal-mass major merger) and two with

Table 1. Parameters of the galaxy encounters, of the progenitor galaxy models and of the merger remnants in the dissipationless binary-merger N -body simulations analyzed in this work. Name: name of simulation. Set: name of the simulation set. M_{DM} : total DM mass. M_{\star} : total stellar mass. c : NFW concentration. r_s : NFW scale radius. R_e : effective radius. $\xi_{\star} = M_{\star,\text{sat}}/M_{\star,\text{main}}$: stellar mass ratio. $r_{\text{peri}}/r_{\text{vir}}$: pericentric-to-virial radius ratio (r_{vir} is the virial radius of the main galaxy), quantifying the orbital angular momentum of the encounter (all encounters are parabolic). A_{IMF} , B_{IMF} and C_{IMF} : parameters used in post-processing to assign α_{IMF} to particles (equations 7 and 8). Here $\tilde{R}_{e,\text{sat}} \equiv R_{e,\text{sat}}/R_{e,\text{main}}$, $\tilde{\sigma}_{e,\text{sat}} \equiv \sigma_{e,\text{sat}}/\sigma_{e,\text{main}}$, $\tilde{\alpha}_{e,\text{sat}} \equiv \alpha_{e,\text{sat}}/\alpha_{e,\text{main}}$, $\tilde{R}_{e,\text{remn}} \equiv R_{e,\text{remn}}/R_{e,\text{main}}$, $\tilde{\sigma}_{e,\text{remn}} \equiv \sigma_{e,\text{remn}}/\sigma_{e,\text{main}}$ and $\tilde{\alpha}_{e,\text{remn}} \equiv \alpha_{e,\text{remn}}/\alpha_{e,\text{main}}$. In all cases $(M_{\text{DM}}/M_{\star})_{\text{main}} = 49$, $c_{\text{main}} = 8$ and $(r_s/R_e)_{\text{main}} = 11.6$. Subscripts ‘main’, ‘sat’ and ‘remn’ refer to the main galaxy, the satellite galaxy and the remnant, respectively.

Name	Set	$(M_{\text{DM}}/M_{\star})_{\text{sat}}$	c_{sat}	$(r_s/R_e)_{\text{sat}}$	ξ_{\star}	$r_{\text{peri}}/r_{\text{vir}}$	A_{IMF}	B_{IMF}	C_{IMF}	$\tilde{R}_{e,\text{sat}}$	$\tilde{R}_{e,\text{remn}}$	$\tilde{\sigma}_{e,\text{sat}}$	$\tilde{\sigma}_{e,\text{remn}}$	$\tilde{\alpha}_{e,\text{sat}}$	$\tilde{\alpha}_{e,\text{remn}}$
1Dh	D	49	8	11.6	1	0	2	0	1	1	2.21	1	1.030	1	0.980
1Do	D	49	8	11.6	1	0.12	2	0	1	1	1.93	1	1.080	1	0.983
1Dh_bis	D	49	8	11.6	1	0	0.5	1	1	1	2.21	1	1.030	1	0.995
1Do_bis	D	49	8	11.6	1	0.12	0.5	1	1	1	1.93	1	1.080	1	0.996
0.5Dh	D	49	8	11.6	0.5	0	2	0	0.95	0.66	1.96	0.870	0.977	0.950	0.962
0.5Do	D	49	8	11.6	0.5	0.2	2	0	0.95	0.66	1.59	0.870	1.036	0.950	0.966
0.2Dh	D	49	8	11.6	0.2	0	2	0	0.895	0.38	1.65	0.746	0.917	0.895	0.971
0.2Do	D	49	8	11.6	0.2	0.2	2	0	0.895	0.38	1.38	0.746	0.983	0.895	0.973
0.2D3h	D3	35	8.5	8.8	0.2	0	2	0	0.935	0.38	1.73	0.758	0.906	0.903	0.970
0.2D3o	D3	35	8.5	8.8	0.2	0.2	2	0	0.935	0.38	1.40	0.758	0.981	0.903	0.972
0.2D4h	D4	75	8.5	15.0	0.2	0	2	0	0.85	0.38	1.61	0.739	0.917	0.892	0.973
0.2D4o	D4	75	8.5	15.0	0.2	0.2	2	0	0.85	0.38	1.36	0.739	0.980	0.892	0.973

$\xi_{\star} = 0.2$ (minor² merger). Here $M_{\star,\text{main}}$ is the stellar mass of the more massive progenitor galaxy (hereafter referred to as *main* galaxy) and $M_{\star,\text{sat}} \leq M_{\star,\text{main}}$ is the stellar mass of the less massive progenitor galaxy (hereafter referred to as *satellite* galaxy). Throughout the paper the subscripts ‘main’, ‘sat’ and ‘remn’ indicate quantities relative to the main galaxy, to the satellite galaxy, and to the merger remnant, respectively.

The main galaxy is modelled as a two-component spherically symmetric stellar system with a stellar component and a dark matter (DM) halo. This model is described in Section 2.2. In the case of equal-mass mergers ($\xi_{\star} = 1$) the satellite galaxy is identical to the main galaxy. In the case of unequal-mass mergers ($\xi_{\star} < 1$) of set D, the satellite galaxy is a smaller-scale replica of the main galaxy, i.e. it is structurally and kinematically homologous (see e.g. section 5.4 of Cimatti et al. 2019) to the main galaxy, but has different mass and length scale, depending on ξ_{\star} (see Section 2.2). In the simulations of set D3 and D4 (all with $\xi_{\star} = 0.2$) the satellite galaxy is not homologous to the main galaxy (see Section 2.2).

In all the simulations considered here the mergers are parabolic (i.e. with zero orbital energy in the point-mass two-body approximation of the encounter). For each value of ξ_{\star} and each set (D, D3 and D4), we have two simulations, one with zero orbital angular momentum ($r_{\text{peri}} = 0$; hereafter referred to as *head-on* merger simulations) and the other with non-zero orbital angular momentum ($r_{\text{peri}} \neq 0$; hereafter referred to as *off-axis* merger simulations), where r_{peri} is the pericentric radius. In Table 1, where the main parameters of the simulations are reported, the orbital angular momentum is quantified by the ratio $r_{\text{peri}}/r_{\text{vir}}$, where r_{vir} is the virial radius of the main galaxy. We note that the values of $r_{\text{peri}}/r_{\text{vir}}$ adopted for our off-axis merger simulations are close to the median values found for halo-halo mergers in cosmological simulations (e.g. Wetzel 2011), which suggests that the off-axis simulations could be more representative of cosmologically motivated mergers than the head-on simulations. For further details on the set-up of the initial condition we refer the reader to Sonnenfeld et al. (2014) and previous papers (Nipoti et al. 2009, 2012) from which some simulations were collected.

² Mergers are usually classified as minor when the mass ratio is lower than either 1/3 or 1/4.

2.2 Progenitor galaxy models

The stellar density distribution of the progenitor galaxies is represented by a γ model (Dehnen 1993; Tremaine et al. 1994) with $\gamma = 3/2$:

$$\rho_{\star}(r) = \frac{3}{8\pi} \frac{M_{\star} r_{\star}}{r^{3/2} (r + r_{\star})^{5/2}}, \quad (3)$$

where M_{\star} is the total stellar mass and r_{\star} is the characteristic radius of the stellar component. The DM halo is described by a Navarro, Frenk & White (1996, NFW) model, so the DM density distribution is

$$\rho_{\text{DM}}(r) = \frac{M_{\text{DM},0}}{r(r + r_s)^2} \exp\left[-\left(\frac{r}{r_{\text{vir}}}\right)^2\right], \quad (4)$$

where r_s is the scale radius, $M_{\text{DM},0}$ is a reference mass and we adopt an exponential cut-off to truncate the distribution smoothly at the virial radius r_{vir} , so the total DM mass $M_{\text{DM}} = 4\pi \int_0^{\infty} \rho_{\text{DM}}(r) r^2 dr$ is finite. We assume Osipkov-Merritt (Osipkov 1979; Merritt 1985) anisotropy in the velocity distribution of the stellar component, whose distribution function is then given by

$$f(Q) = \frac{1}{\sqrt{8\pi^2}} \frac{d}{dQ} \int_0^Q \frac{d\varrho_{\star}}{d\Psi_{\text{tot}}} \frac{d\Psi_{\text{tot}}}{\sqrt{Q - \Psi_{\text{tot}}}}, \quad (5)$$

where

$$\varrho_{\star}(r) = \left(1 + \frac{r^2}{r_a^2}\right) \rho_{\star}(r). \quad (6)$$

The variable Q is defined as $Q \equiv \mathcal{E} - L^2/2r_a^2$, where the relative (positive) energy is given by $\mathcal{E} = \Psi_{\text{tot}} - v^2/2$, v is the modulus of the velocity vector, the relative (positive) total potential is $\Psi_{\text{tot}} = \Psi_{\star} + \Psi_{\text{DM}}$ (Ψ_{\star} and Ψ_{DM} are, respectively, the relative potentials of the stellar and DM components), L is the angular momentum modulus per unit mass, and $f(Q) = 0$ for $Q \leq 0$. The quantity r_a is the so-called anisotropy radius: for $r \gg r_a$ the velocity dispersion tensor is radially anisotropic, while for $r \ll r_a$ the tensor is nearly isotropic. In the limit $r_a \rightarrow \infty$, $Q = \mathcal{E}$ and the velocity dispersion tensor is globally isotropic.

The orbital distribution of the DM halo is assumed isotropic, so the distribution function of the DM component is given by equation (5) where $Q = \mathcal{E}$ and $\rho_{\text{DM}}(r)$ substitutes $\varrho_{\star}(r)$. These

$\gamma = 3/2$ plus NFW models have four free parameters: the concentration $c \equiv r_{\text{vir}}/r_s$, the dark-to-stellar mass ratio M_{DM}/M_* , the ratio $\tilde{r}_s \equiv r_s/R_e$ and the anisotropy radius r_a . We consider different choices of these parameters for the progenitor galaxies of our mergers. When building the progenitor galaxies (both main and satellite) of set D we assume $c = 8$, $M_{\text{DM}}/M_* = 49$, $\tilde{r}_s = 11.6$ and $r_a/r_* = 1$. In set D3 and D4 the main galaxy is identical to that of set D, but the satellite has different values of the parameters: $c = 8.5$, $M_{\text{DM}}/M_* = 35$, $\tilde{r}_s = 8.8$ and $r_a/r_* = 1$ for set D3, and $c = 8.5$, $M_{\text{DM}}/M_* = 75$, $\tilde{r}_s = 15$ and $r_a/r_* = 1$ for set D4. The values of the parameters are such that the galaxy models are realistic for massive ETGs (Nipoti et al. 2009; Sonnenfeld et al. 2014). In all the runs $R_{e,\text{sat}}/R_{e,\text{main}} = \xi_*^a$ and $\sigma_{e,\text{sat}}/\sigma_{e,\text{main}} = \xi_*^b$ with $a \simeq 0.6$ and $b \simeq 0.2$, so the satellites and the main galaxies lie on R_e - M_* and σ_e - M_* relations with slopes similar to those observed for massive ETGs (e.g. Cimatti et al. 2012; van der Wel et al. 2014; Cannarozzo et al. 2020).

2.3 Parameters of the N -body simulations

All the binary-merger N -body simulations were run with the collisionless N -body code FVFPs (Fortran Version of a Fast Poisson Solver; Londrillo et al. 2003; Nipoti et al. 2003a). Stellar and dark matter particles have the same mass in runs with $\xi_* = 1$; when $\xi_* < 1$ the dark matter particles are twice as massive as the stellar particles. The total number of particles used in each simulation is in the range $1.6 \times 10^6 - 3.1 \times 10^6$. The parameters of the simulations are given in Nipoti et al. (2009), Nipoti et al. (2012) and Sonnenfeld et al. (2014). In all the simulations the galaxy encounter is followed up to the virialisation of the resulting stellar system. We define the merger remnant as the system composed by the bound stellar and dark matter particles at the end of the simulation.

3 ANALYSIS OF THE SIMULATIONS

3.1 Assigning α_{IMF} to stellar particles

Given that the distribution function of the stellar component of each progenitor galaxy depends on the integral of motion Q , we can build a stationary galaxy model with a gradient in a stellar population property, say metallicity Z , by assigning to each particle a value of Z as a function of Q (Ciotti et al. 1995; see also Nipoti et al. 2003b). Here we are interested in α_{IMF} gradients, thus we assign a value of α_{IMF} to each particle in each progenitor galaxy as a function of Q . Let us consider a binary merger between the main galaxy of stellar mass $M_{*,\text{main}}$ and the satellite of stellar mass $M_{*,\text{sat}} \leq M_{*,\text{main}}$.

In order to assign a value of α_{IMF} to particles belonging to the main galaxy, we adopt the linear relation

$$\alpha_{\text{IMF}}(Q) = A_{\text{IMF}}\tilde{Q} + B_{\text{IMF}}, \quad (7)$$

where $\tilde{Q} \equiv Q/\Psi_{\text{tot},0}$ and $\Psi_{\text{tot},0} \equiv \Psi_{\text{tot}}(0)$, where Ψ_{tot} is the relative total potential of the main galaxy. For particles belonging to the satellite galaxy, we assume

$$\alpha_{\text{IMF}}(Q) = C_{\text{IMF}} \times (A_{\text{IMF}}\tilde{Q} + B_{\text{IMF}}), \quad (8)$$

where A_{IMF} and B_{IMF} have the same values as for the main galaxy, $\tilde{Q} \equiv Q/\Psi_{\text{tot},0}$ and $\Psi_{\text{tot},0} \equiv \Psi_{\text{tot}}(0)$, where now Ψ_{tot} is the relative total potential of the satellite progenitor galaxy. In the special case of equal-mass mergers ($\xi_* = 1$), we always adopt $C_{\text{IMF}} = 1$; for

unequal-mass mergers ($\xi_* < 1$), $C_{\text{IMF}} < 1$, i.e. the satellite has, on average, lighter IMF than the main galaxy. We further assume that during the simulation each particle maintains its value of α_{IMF} unaltered. Thus, given the above assumptions, in each binary merger we have three free dimensionless parameters to assign α_{IMF} to the particles: A_{IMF} , B_{IMF} and C_{IMF} . Clearly, the values of A_{IMF} , B_{IMF} and C_{IMF} do not influence the dynamical evolution of the simulation, and can be assumed a posteriori. It follows that, as far as the distribution of α_{IMF} is concerned, each of the considered merging simulations can be formally interpreted in infinite different ways by choosing the values of A_{IMF} , B_{IMF} and C_{IMF} in post-processing. We stress that the specific forms of equations (7) and (8) are not theoretically justified, but are just simple functions of Q that allow us to obtain α_{IMF} profiles similar to those measured in real ETGs (see also Ciotti et al. 1995 and Nipoti et al. 2003b). Clearly, α_{IMF} could be also assigned to particles using functions different from equations (7) and (8), for instance higher-degree polynomials of \tilde{Q} , but we found that the prescriptions (7) and (8) are sufficiently general for the purpose of the present investigation (see Section 4).

3.2 Diagnostics

3.2.1 Spherical systems

Before considering the analysis of the N -body systems of our simulations (both progenitor galaxies and merger remnants), it is useful to define a few relevant projected quantities for a spherical galaxy model with stellar distribution function $f(Q)$. The stellar mass surface density profile is

$$\Sigma(R) = \int f(Q) dx_{\text{los}} d^3v, \quad (9)$$

where x_{los} is a coordinate along the line of sight and R is the projected radius. The effective radius R_e is the projected radius of a circle containing half of the stellar mass, such that

$$2\pi \int_0^{R_e} \Sigma(R) R dR = \frac{M_*}{2}. \quad (10)$$

The line-of-sight stellar velocity dispersion profile $\sigma_{\text{los}}(R)$ is defined by

$$\sigma_{\text{los}}^2(R) = \frac{1}{\Sigma(R)} \int f(Q) (v_{\text{los}} - \bar{v}_{\text{los}})^2 dx_{\text{los}} d^3v, \quad (11)$$

where v_{los} is the line-of-sight velocity, \bar{v}_{los} is the mean of v_{los} and \mathbf{v}_R is a vector representing the velocity components in the plane of the sky. The effective velocity dispersion, i.e. the stellar mass-weighted line-of-sight central stellar velocity dispersion measured within a circle of radius R_e , is given by

$$\sigma_e^2 = \frac{2\pi \int_0^{R_e} \Sigma(R) \sigma_{\text{los}}^2(R) R dR}{M_*/2}. \quad (12)$$

We note that σ_e in observed galaxies is a luminosity-weighted quantity, while here for simplicity we have defined it for our galaxy models as a mass-weighted quantity. Strictly speaking, the two definitions differ because we are considering systems with gradients in α_{IMF} and thus in M_*/L (see Bernardi et al. 2018), but this difference is expected to be small, especially for our models in which σ_{los} varies at most by $\approx 20\%$ at $R \leq R_e$ (Section 4.1). The projected α_{IMF} profile is

$$\alpha_{\text{IMF}}(R) = \frac{1}{\Sigma(R)} \int \alpha_{\text{IMF}}(Q) f(Q) dx_{\text{los}} d^3v. \quad (13)$$

We define the effective IMF mismatch parameter as the mass-weighted projected α_{IMF} within R_e , i.e.

$$\alpha_e = \frac{2\pi \int_0^{R_e} \Sigma(R) \alpha_{\text{IMF}}(R) R dR}{M_*/2}. \quad (14)$$

3.2.2 N -body systems

The projected properties of our N -body models are computed as in Nipoti et al. (2006) and Nipoti et al. (2009). In particular, for any given line of sight, having determined the ellipticity ϵ and the principal axes of the stellar surface density distribution, we measure all the projected quantities considering concentric elliptical annuli all with the same ellipticity ϵ . The k -th annulus is characterized by its average circularized radius R_k , such that $\log R_{k+1} - \log R_k = \Delta x$ with $\Delta x = \text{constant}$ for all k . The effective radius R_e is computed as the circularized radius of the ellipse containing half of the stellar particles in projection. The line-of-sight velocity dispersion at R_k is computed as

$$\sigma_{\text{los}}(R_k) = \left[\frac{1}{N_k} \sum_i (v_{\text{los},i} - \bar{v}_{\text{los},k})^2 \right]^{1/2}, \quad (15)$$

where $v_{\text{los},i}$ is the line-of-sight velocity dispersion of the i -th particle, the sum is over all the N_k stellar particles belonging to the k -th projected annulus and $\bar{v}_{\text{los},k}$ is the mean line-of-sight velocity of these N_k particles (the total number of stellar particles is $N = \sum_k N_k$). The effective velocity dispersion is computed as

$$\sigma_e = \left[\frac{2}{N} \sum_i (v_{\text{los},i} - \bar{v}_{\text{los}})^2 \right]^{1/2}, \quad (16)$$

where \bar{v}_{los} is the mean line-of-sight velocity of the $N/2$ stellar particles contained within the ellipse with circularized radius R_e and the sum is over the same $N/2$ particles.

We compute the radial profile of the IMF mismatch parameter as

$$\alpha_{\text{IMF}}(R_k) = \frac{1}{N_k} \sum_i \alpha_{\text{IMF},i}, \quad (17)$$

where $\alpha_{\text{IMF},i}$ is the value of α_{IMF} of the i -th particle, and the sum is over all the N_k stellar particles belonging to the k -th annulus. The effective IMF mismatch parameter is computed as

$$\alpha_e = \frac{2}{N} \sum_i \alpha_{\text{IMF},i}, \quad (18)$$

where the sum is over all the $N/2$ stellar particles contained within the ellipse with circularized radius R_e .

For each N -body system we consider 50 projections with different (random) lines of sight and we compute the mean and standard deviation of $\sigma_{\text{los}}(R_k/R_e)$, σ_e , $\alpha_{\text{IMF}}(R_k/R_e)$ and α_e .

3.3 Physical units and normalizations

Given the scale-free nature of gravity, our dissipationless merging simulations are fully scalable in mass and length. We take as mass unit $M_u = M_{*,\text{main}}$ the stellar mass of the main galaxy and as length unit $\ell_u = r_{*,\text{main}}$ the stellar scale radius of the main galaxy. Thus, for the adopted main galaxy model (Section 2.2), the effective radius of the main galaxy is

$$R_{e,\text{main}} \simeq 1.23 \left(\frac{\ell_u}{\text{kpc}} \right) \text{kpc} \quad (19)$$

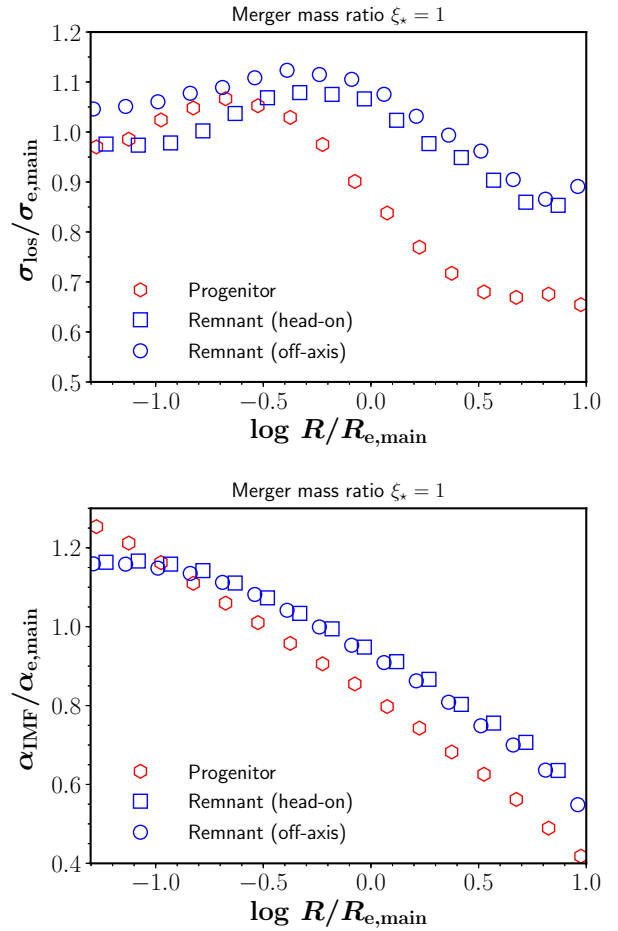


Figure 1. Angle-averaged line-of-sight velocity dispersion (upper panel) and IMF mismatch parameter (lower panel) profiles of the remnants of the equal-mass merging simulations 1Dh (squares) and 1Do (circles), and of their progenitor galaxies (hexagons). $R_{e,\text{main}}$, $\sigma_{e,\text{main}}$ and $\alpha_{e,\text{main}}$ are, respectively, the effective radius, velocity dispersion and IMF mismatch parameter of the progenitor galaxies.

and the effective velocity dispersion of the main galaxy is

$$\sigma_{e,\text{main}} \simeq 92.9 \left(\frac{M_u}{10^{10} M_\odot} \right)^{1/2} \left(\frac{\ell_u}{\text{kpc}} \right)^{-1/2} \text{km s}^{-1}. \quad (20)$$

As far as the IMF mismatch parameter is concerned, we normalize all our results to $\alpha_{e,\text{main}}$, the value of α_e of the main galaxies. The value of $\alpha_{e,\text{main}}$ is independent of both M_u and ℓ_u , and can be chosen freely if one wants to apply our results to specific observational targets. We recall that for an ensemble of stellar particles, the quantity α_{IMF} used in this paper is the true M_*/L normalized to the M_*/L of a reference IMF (equation 1). Our results can be interpreted by choosing freely the reference IMF: for instance a Salpeter, a Kroupa or a Chabrier IMF.

4 RESULTS

Here we present the results on the evolution of α_{IMF} in mergers based on the dissipationless binary merging simulations described in Section 2. In order to assign values of α_{IMF} to particles, we have to choose, in post-processing, the values of the coefficients

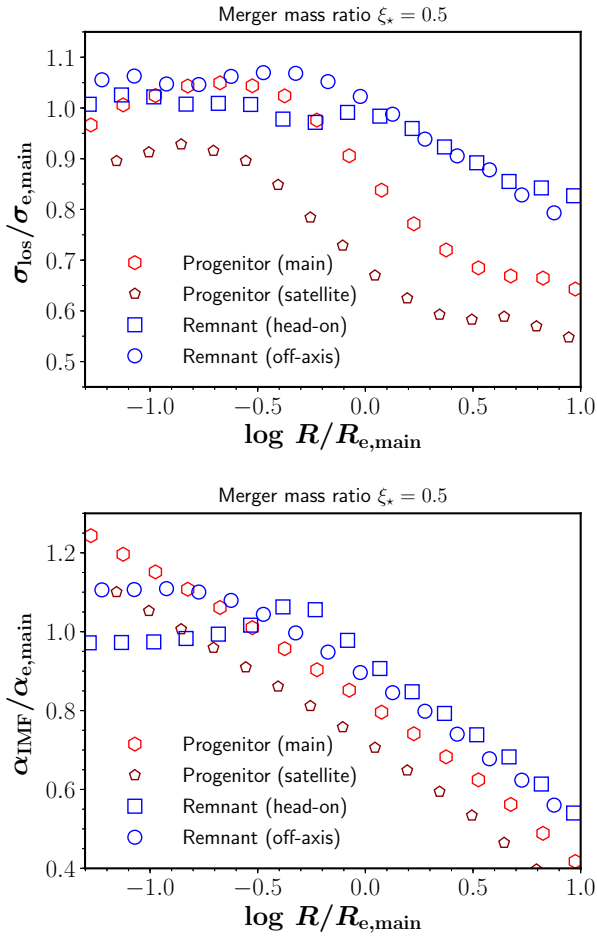


Figure 2. Same as Fig. 1, but for the merging simulations with stellar mass ratio $\xi_* = 0.5$. The hexagons and pentagons represent, respectively, the main and satellite progenitor galaxies. The remnants are indicated with squares (simulation 0.5Dh) and circles (simulation 0.5Dh). $R_{e,\text{main}}$, $\sigma_{e,\text{main}}$ and $\alpha_{e,\text{main}}$ are, respectively, the effective radius, velocity dispersion and IMF mismatch parameter of the main progenitor galaxy.

A_{IMF} , B_{IMF} and C_{IMF} (Section 3.1). We present here results obtained adopting $A_{\text{IMF}} = 2$, $B_{\text{IMF}} = 0$ and C_{IMF} that depends on ξ_* (the specific values of C_{IMF} are reported in Table 1). In Sections 4.2 and 4.3 we show that with this choice we obtain progenitor galaxy models with realistic α_{IMF} profiles. We experimented with different choices of the values of A_{IMF} , B_{IMF} and C_{IMF} , finding that, provided that the values give realistic α_{IMF} profiles in the progenitors, the merger-driven evolution of the α_{IMF} profiles is weakly dependent on the specific choice of A_{IMF} , B_{IMF} and C_{IMF} . In Appendix A, we show examples illustrating the effect of choosing values of A_{IMF} and B_{IMF} giving significantly different α_{IMF} profiles for the progenitors. The results presented in this section refer to simulations (set D in Table 1) in which the main and satellite galaxies are structurally and dynamically homologous (see Section 2.1). In Appendix B we compare some of these simulations with analogous simulations in which the satellite and the progenitor galaxies are not homologous, finding results very similar to those presented in this section.

The profiles of σ_{los} and α_{IMF} , as well as the integrated quantities σ_e and α_e , depend on the line of sight. In this section, we show for each N -body system a single value of each of these quantities, that is the mean over 50 different lines of sight. In some cases we

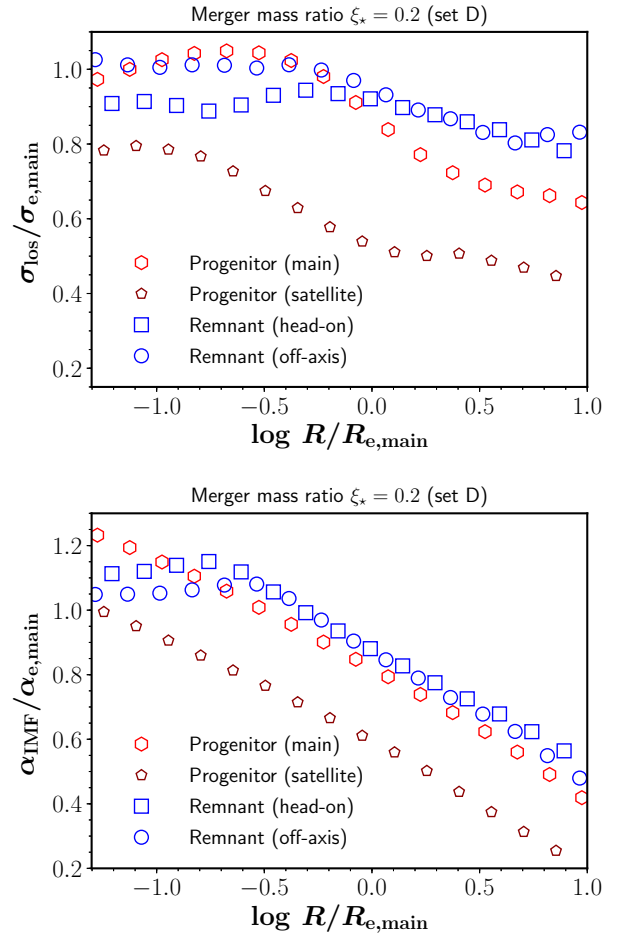


Figure 3. Same as Fig. 2, but for the remnants of the $\xi_* = 0.2$ merging simulations with stellar mass ratio 0.2D3h (squares) and 0.2D3o (circles), and for their main (hexagons) and satellite (pentagons) progenitor galaxies.

associate to this mean, as an error bar, the corresponding standard deviation (see Section 3.2.2).

4.1 Velocity dispersion profiles

The stellar line-of-sight velocity dispersion profiles of the progenitor galaxies and of the remnants of the simulations are shown in the upper panels of Figs. 1-3. In the main galaxy (hexagons in the plots) σ_{los} increases from the centre out to $\approx 0.25R_e$, where it peaks, and decreases outwards at larger radii out to $\approx 10R_e$. The positive inner gradient of σ_{los} is usually not observed in real ETGs (e.g. de Zeeuw et al. 2002; Falc3n-Barroso et al. 2017), but we note that in our model such a positive gradient is limited to very small radii ($R \lesssim 0.2R_e$), not always probed in spectroscopic observations. In fact, the inner σ_{los} profile of the progenitors is very shallow (σ_{los} increases by $\approx 10\%$ from $R \approx 0.02R_e$ to $R \approx 0.2R_e$), so we do not expect this feature of our progenitor galaxy models to affect the main conclusions of our work. From the peak to R_e , the decrease in σ_{los} is about 20%, broadly consistent with the observed profiles of ETGs (see e.g. Raskutti et al. 2014; Veale et al. 2018). The satellite galaxies in the unequal-mass mergers (pentagons in Figs. 2-3) are homologous to the main galaxy, so they have σ_{los} profiles with the same shape as that of the main, but just scaled down to lower values of velocity dispersion.

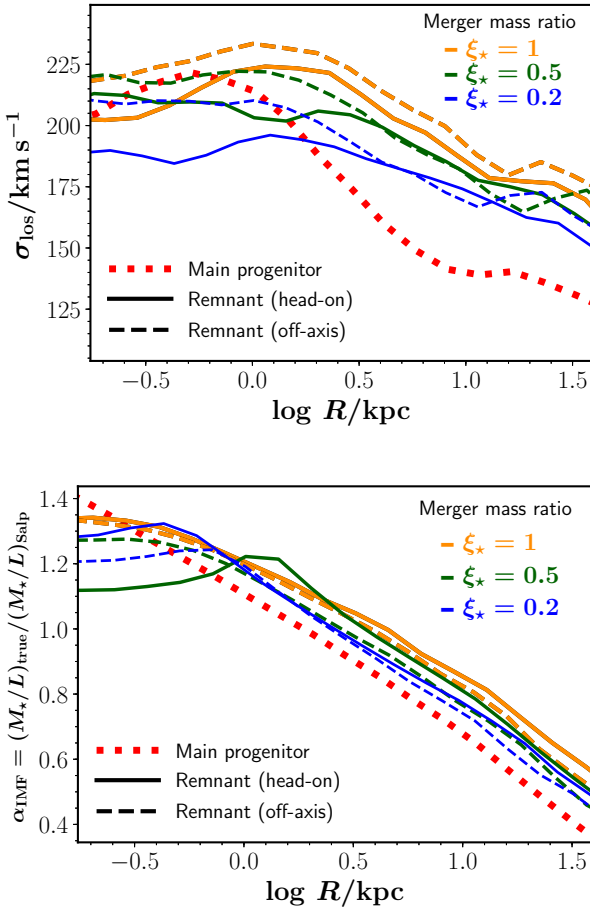


Figure 4. Angle-averaged line-of-sight velocity dispersion (upper panel) and IMF mismatch parameter (lower panel) profiles of the remnants of the head-on (solid curves) and off-axis (dashed curves) merging simulations, and of their main progenitor galaxy (dotted curve) in physical units, assuming mass unit $M_u = 10^{11} M_\odot$, length unit $\ell_u = 2$ kpc (so $M_{*,\text{main}} = 10^{11} M_\odot$, $R_{e,\text{main}} \approx 2.5$ kpc and $\sigma_{e,\text{main}} \approx 208$ km s $^{-1}$; see Section 3.3) and $\alpha_{e,\text{main}} = 1.15$, taking as reference the Salpeter IMF. The curves representing the remnants are thicker for higher merger mass ratio ($\xi_* = 1$, orange curves; $\xi_* = 0.5$, green curves; $\xi_* = 0.2$, blue curves).

The remnants of the equal-mass mergers (Fig. 1) have line-of-sight velocity dispersion comparable to or higher than that of the progenitors at all radii: we find that σ_{los} increases more in the off-axis than in the head-on merger, as found in general in dissipationless mergers (e.g. Boylan-Kolchin et al. 2006; Nipoti et al. 2009). The remnants of unequal-mass mergers (Figs. 2-3) have lower σ_{los} profiles than those of the equal-mass mergers. The lowest σ_{los} profile is obtained for the remnant of the head-on minor merger ($\xi_* = 0.2$). Focusing on the central parts of the velocity dispersion profiles, we notice that the behaviour of σ_{los} in the remnant ranges from being higher (as in the off-axis $\xi_* = 1$ merger) to being lower (as in the head-on $\xi_* = 0.2$ merger) than σ_{los} in the main progenitor.

In Figs. 1-3 σ_{los} and R are normalized, respectively, to the effective velocity dispersion $\sigma_{e,\text{main}}$ and to the effective radius $R_{e,\text{main}}$ of the main progenitor galaxy for both the progenitors and the remnants, so all the σ_{los} profiles are shown on the same physical scale. These profiles can be converted in physical units by fixing M_u

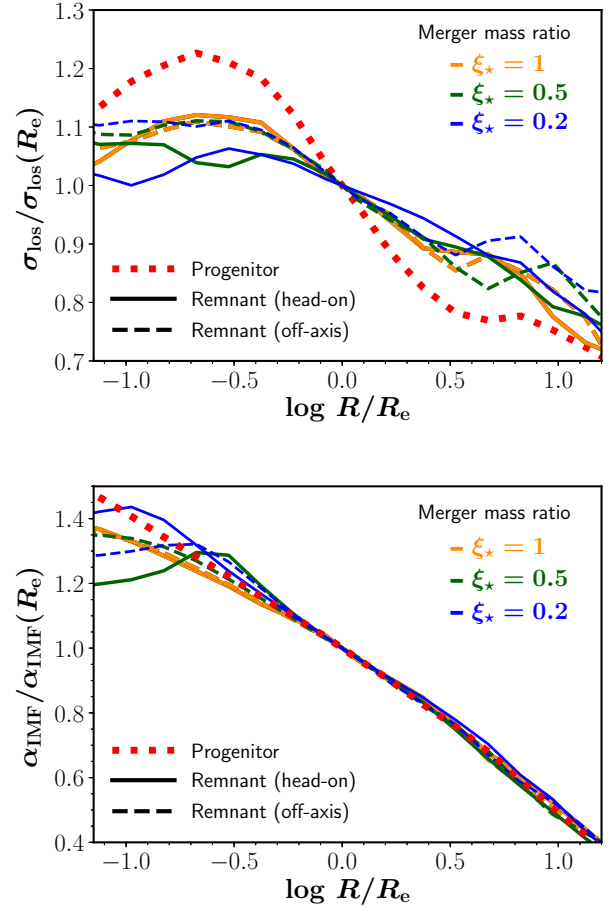


Figure 5. Same as Fig. 4, but here the profiles are normalized to the values of σ_{los} and α_{IMF} at the effective radius R_e ($R_e = R_{e,\text{main}}$ for the main progenitor and $R_e = R_{e,\text{remn}}$ for the remnants).

and ℓ_u (see Section 3.3): an example is given in the upper panel of Fig. 4, showing the σ_{los} profiles of the main progenitor and of the remnants of the same six simulations as in Figs. 1-3. When interpreting the variations in the σ_{los} profiles shown in Figs. 1-4 one must bear in mind that, as well known, dry mergers make galaxies more diffuse (see values of $\tilde{R}_{e,\text{remn}}$ in Table 1), so the effect of mergers is not only to change the shape of the σ_{los} profiles, but also to “stretch” them horizontally. To isolate the effect of the mergers on the shape of the σ_{los} profiles, it is useful to normalize R and σ_{los} of each system (either progenitor or remnant) to, respectively, their own R_e and σ_{los} at R_e , as done in the upper panel of Fig. 5. The main effect of the mergers on the shape of the σ_{los} profile is an overall flattening of the profile. We also note that the positive central σ_{los} gradient of the progenitor tends to be erased by the merging.

4.2 Initial mass function mismatch parameter profiles

The stellar IMF mismatch parameter profiles of the progenitor galaxies and of the remnants of the simulations are shown in the lower panels of Figs. 1-3. In the progenitor galaxies (hexagons and pentagons in the plots) α_{IMF} decreases monotonically with radius, by a factor of about two from the centre to $\approx 3R_e$, consistent with the observational estimates of present-day ETGs (e.g. La Barbera et al. 2019). We note that, given that by construction

A_{IMF} and B_{IMF} are the same in the two progenitor galaxies, the α_{IMF} profile of the satellite galaxy (pentagons) is just a scaled-down version of that of the main galaxy (hexagons): specifically, at given R/R_e , $\alpha_{\text{IMF,sat}} = C_{\text{IMF}}\alpha_{\text{IMF,main}}$, with $C_{\text{IMF}} \leq 1$.

Let us focus first on equal-mass mergers (Fig. 1). The merger remnant has, with respect to the progenitor galaxies, a shallower central gradient of α_{IMF} . The remnant's α_{IMF} profile is very similar for off-axis (circles) and head-on (squares) encounters. Moving to unequal-mass major ($\xi_* = 0.5$; Fig. 2) and minor ($\xi_* = 0.2$; Fig. 3) mergers, we note that the main effect of the merger is to flatten the central gradient of α_{IMF} by producing a central 'core' of constant α_{IMF} with size ranging from ≈ 0.1 to ≈ 0.3 in units of $R_{e,\text{main}}$. The core is produced by the lower- α_{IMF} stellar particles of the satellite that settle in the central regions and mix with the higher- α_{IMF} stellar particles of the main. For major mergers ($\xi_* = 0.5$) the core is larger for head-on (squares) than for off-axis (circles) encounters, while for minor mergers ($\xi_* = 0.2$) the core is larger for off-axis than for head-on encounters, which suggests that mixing and accretion of satellite's stars in the central region of the remnant depends in a non-trivial way both on the orbit of the encounter and on the merger mass ratio, for given structural properties of the progenitors.

The α_{IMF} profiles shown in Figs. 1-3 are all on the same physical scale, because α_{IMF} and R are normalized, respectively, to the effective IMF mismatch parameter $\alpha_{e,\text{main}}$ and to effective radius $R_{e,\text{main}}$ of the main progenitor. In the lower panel of Fig. 4, the α_{IMF} profiles of the main progenitor and of the remnants are shown in physical units, for a representative case in which we have assumed $\alpha_{e,\text{main}} = 1.15$ and the Salpeter IMF as reference. As done for the σ_{los} profiles (Section 4.1), in Fig. 5 (lower panels) we show the same α_{IMF} profiles as in Fig. 4, but normalized to R_e and $\sigma_{\text{los}}(R_e)$, to highlight the variations in the shape of the profiles, which are significant only at $R \leq R_e$. In Figs. 1-4 the remnants have higher α_{IMF} than the progenitor at large radii mainly because of the merger-driven size evolution: on average, stars originally belonging to the main progenitor orbit at larger (physical) radius in the remnant.

Overall, under the considered hypotheses (heavier average IMF in more massive progenitors and negative radial gradients of α_{IMF} in the progenitors), the effect of dissipationless mergers is invariably to redistribute α_{IMF} by reducing it in the central regions and slightly increasing it at larger radii, thus weakening the α_{IMF} gradient. We note that this weakening of the α_{IMF} gradient is not a necessary consequence of merging with a lower- α_{IMF} satellite, but it must be expected when the α_{IMF} gradient in the main progenitor is sufficiently strong and when the satellite is sufficiently compact not to be completely disrupted in the outskirts of the main. If the main progenitor had a negligible α_{IMF} gradient, a merger with a low α_{IMF} satellite could give rise to α_{IMF} profiles with both positive and negative α_{IMF} gradients (see Section 1). The effect of dry merging on the α_{IMF} profiles depends also on the structural properties of the satellite (see Section 4.5.1). The accretion of loose (low-density) satellites with low α_{IMF} can produce a negative radial gradient of α_{IMF} , because such satellites tend to deposit their stars mainly in the outer regions of the remnant, while the central α_{IMF} is determined by stars formed in situ (see Smith 2020, for a discussion).

4.3 Local α_{IMF} as a function of local σ_{los}

In their study of the spatially resolved stellar IMF, Parikh et al. (2018) explored the distribution of the local α_{IMF} as a function of the local σ_{los} for a large sample of ETGs (see figure 16 in that paper; see also Domínguez Sánchez et al. 2019, 2020). Here we perform a similar analysis, but for our merging simulations. In Fig. 6 we

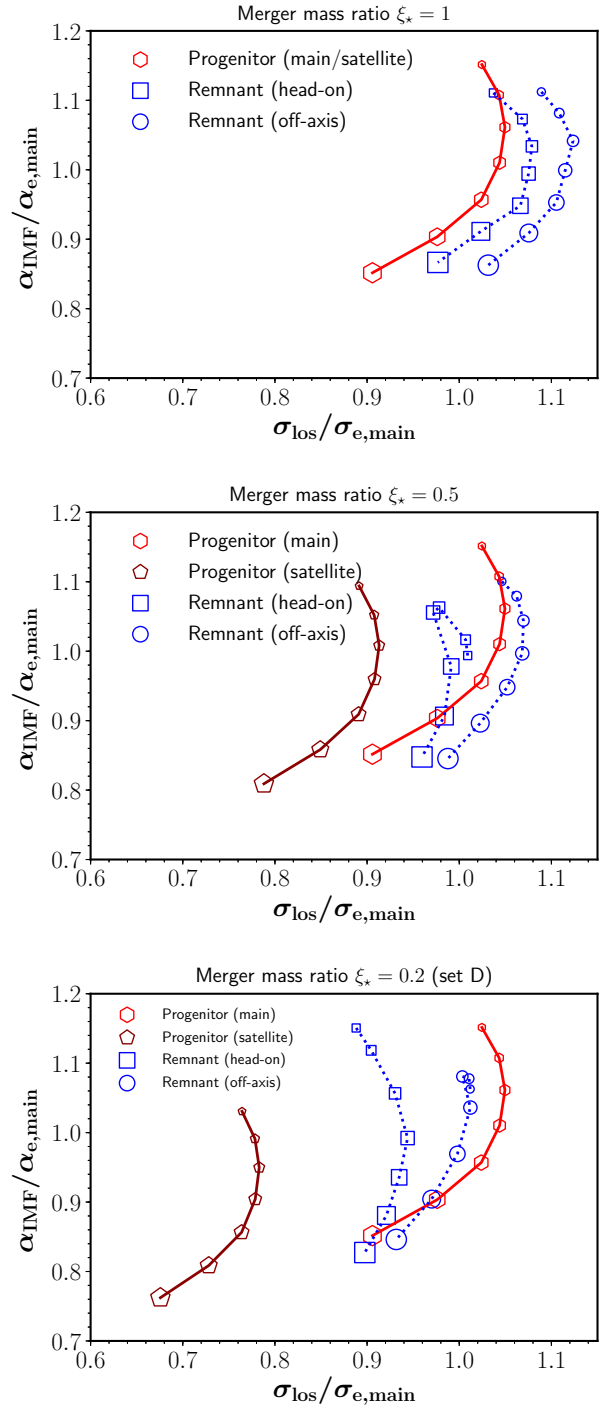


Figure 6. Local (i.e. at given R) IMF mismatch parameter α_{IMF} as a function of local (at the same R) line-of-sight velocity dispersion σ_{los} of the progenitor galaxies and of the remnants of simulations 1Dh and 1Do ($\xi_* = 1$, top panel), 0.5Dh and 0.5Do ($\xi_* = 0.5$, middle panel) and 0.2Dh and 0.2Do ($\xi_* = 0.2$, bottom panel) in the radial interval $0.1 \leq R/R_e \leq 1$, where $R_e = R_{e,\text{main}}$ for the main galaxy, $R_e = R_{e,\text{sat}}$ for the satellite galaxy and $R_e = R_{e,\text{remn}}$ for the remnants. Symbols and normalizations are the same as in Figs. 1-3. The size of the symbol increases for increasing R .

plot the local α_{IMF} as a function of the local σ_{los} for the remnants and the progenitor galaxies of our simulations with $\xi_* = 1$ (top panel), $\xi_* = 0.5$ (middle panel) and $\xi_* = 0.2$ (bottom panel). Similar to Parikh et al. (2018), in these diagrams we plot only values of $\sigma_{\text{los}}(R)$ and $\alpha_{\text{IMF}}(R)$ lying in the radial range $0.1 \lesssim R/R_e \lesssim 1$. The bottom parts of the distributions correspond to $R \approx R_e$ (lower values of α_{IMF}), while the top parts to the central regions (higher α_{IMF}). The $\alpha_{\text{IMF}}-\sigma_{\text{los}}$ distribution of the progenitor galaxies of our simulations is qualitatively similar to that inferred for real ETGs by Parikh et al. (2018), though, quantitatively, the relative variations in σ_{los} and α_{IMF} are somewhat smaller in our model galaxies than in the ETGs of Parikh et al.’s sample. In both model and real ETGs the trend is that α_{IMF} tends to increase with σ_{los} , but, different from the data of Parikh et al. (2018), in our progenitor galaxies the points with the highest α_{IMF} are not those with the highest σ_{los} : this reflects the fact that the σ_{los} profiles of these models peak at $R \approx 0.2R_e$ and slightly decreases towards the centre (Fig. 4). By construction, the distribution of the satellite galaxy in the unequal-mass merger simulations is a scaled-down version of that of the main galaxy.

The $\alpha_{\text{IMF}}-\sigma_{\text{los}}$ distributions of the remnants are qualitatively similar to those of the progenitor galaxies. In detail, the distributions tend to be narrower in σ_{los} , because in the radial range $0.1 \lesssim R/R_e \lesssim 1$ the remnants’ σ_{los} profiles are flatter than those of the progenitors (see upper panel of Fig. 5). Moreover, with the only exception of the $\xi_* = 0.2$ head-on merger, the range in α_{IMF} spanned by the remnants tends to be smaller than that spanned by the progenitors, as a consequence of the mixing of the stellar populations in the central regions. The average σ_{los} of the remnant is higher than that of the main galaxy when $\xi_* = 1$ and lower when $\xi_* = 0.2$. When $\xi_* = 0.5$ the average σ_{los} is comparable to that of the main galaxy, with a behaviour that depends in detail on the orbital angular momentum of the encounter. We note that the remnant of the head-on $\xi_* = 0.5$ major merger has a peculiar distribution in the $\sigma_{\text{los}}\alpha_{\text{IMF}}$ plane (squares in the middle panel of Fig. 6), which reflects the somewhat unusual σ_{los} and α_{IMF} profiles (squares in Fig. 2). In this case the satellite reaches and modifies the central regions of the main, both inducing mixing in the existing stellar populations and depositing its own stars. The effect is strongest for intermediate mass ratios ($\xi_* = 0.5$), because for higher mass ratios ($\xi_* = 1$) the progenitors have the same average α_{IMF} and for lower mass ratios ($\xi_* = 0.2$) the satellite carries a small fraction of the total stellar mass of the remnant. However, encounters with exactly zero orbital angular momentum are extreme cases, and we expect the off-axis simulations, which produce more regular distributions of σ_{los} and α_{IMF} , to be more realistic (see Section 2.1).

We note that in figure 16 of Parikh et al. (2018), which is based on a sample of present-day ETGs, more massive galaxies have higher average σ_{los} , as it is usual. In our minor merger simulations (bottom panel of Fig. 6) the remnants have lower average σ_{los} than their main progenitors, which are naturally less massive. This result is not necessarily in contrast with the observational data, because it must be put in the context of galaxy evolution (see Sections 4.4-4.5): we recall that the observed M_*/σ_e relation of ETGs evolves with redshift in the sense that, at given M_* , σ_e tends to be higher at higher z (see Cannarozzo et al. 2020, and references therein).

4.4 Effect of dry mergers on σ_e and α_e

We move here to study the effect of the considered dissipationless mergers on the global galaxy properties: the effective IMF mismatch parameter α_e and the effective velocity dispersion σ_e .

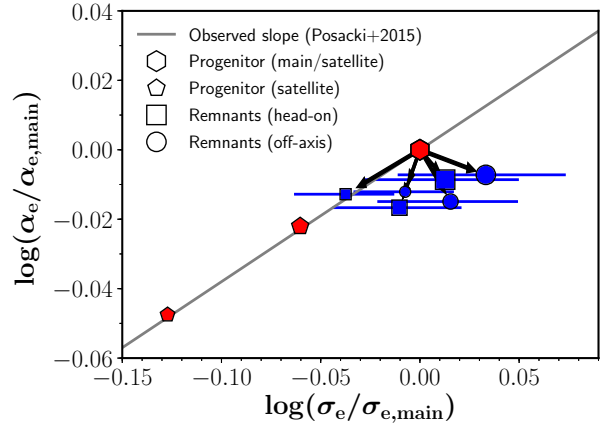


Figure 7. Effective IMF α_e (normalized to α_e of the main progenitor galaxy) as a function of effective velocity dispersion σ_e (normalized to σ_e of the main galaxy) for the remnants of simulations 1Dh (head-on, $\xi_* = 1$), 1Do (off axis, $\xi_* = 1$), 0.5Dh (head-on, $\xi_* = 0.5$), 0.5Do (off axis, $\xi_* = 0.5$), 0.2Dh (head-on, $\xi_* = 0.2$) and 0.2Do (off axis, $\xi_* = 0.2$), and of their main (hexagons) and satellite (pentagons) progenitor galaxies (in the case $\xi_* = 1$ the satellite progenitor galaxy is identical to the main galaxy, and both are represented by the hexagon). The remnants of head-on and off-axis merging simulations are represented, respectively, by squares and circles, whose size is larger for higher stellar-mass ratios ξ_* . The error bars indicate 1σ scatter on the effective velocity dispersion due to projection effects on the remnants (the 1σ scatter in effective IMF mismatch parameter is comparable to or smaller than the symbol size). The arrows connect the position of the main galaxy with those of the remnants and thus indicate the transformations produced by the mergers on the main galaxy. The grey line indicates the slope of the observational $\alpha_e-\sigma_e$ relation as determined by Posacki et al. (2015) for a sample of present-day ETGs (equation 2). We note that the scatter of the observational relation, 0.12 dex in α_e at given σ_e , is comparable to extent of the vertical axis of the plot.

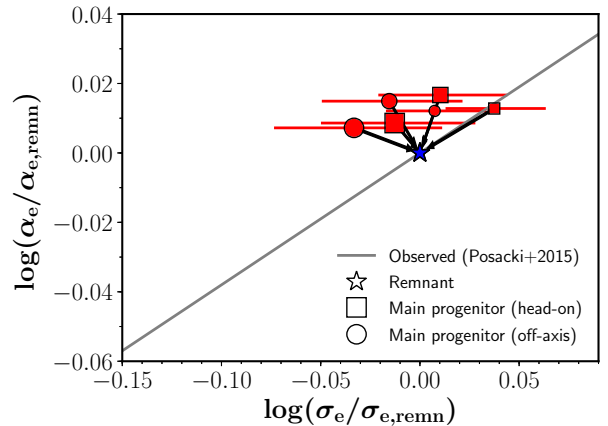


Figure 8. Same as Fig. 7, for the same simulations, but now α_e and σ_e are normalized to values $\alpha_{e,\text{remn}}$ and $\sigma_{e,\text{remn}}$ measured for the remnants. By definition the remnant, represented by a star, lies at $\sigma_e/\sigma_{e,\text{remn}} = 1$ and $\alpha_e/\alpha_{e,\text{remn}} = 1$. The progenitors are indicated with squares for head-on mergers and circles for off-axis mergers, of size increasing with ξ_* . Error bars on the positions of the main progenitors are due to 1σ projection-effect scatter on the remnant’s effective velocity dispersion. Here the satellite galaxies are not shown. The grey solid line indicates the observed present-day $\alpha_e-\sigma_e$ relation (equation 2). The arrows have the same role as in Fig. 7.

Fig. 7 shows the behaviour of our simulations in the $\sigma_e\alpha_e$ plane in which α_e is normalized to $\alpha_{e,\text{main}}$ and σ_e to $\sigma_{e,\text{main}}$. By construction (i.e. as a consequence of our choice of the parameter C_{IMF}), the main galaxy (hexagon) and the satellite galaxies (pentagons) lie on a power law $\alpha_e \propto \sigma_e^{0.38}$ with the same slope as the correlation (equation 2) observed for present-day ETGs. The remnants (squares and circles with error bars) have in all cases α_e lower than that of the main progenitor, which is an expected consequence of the flattening of the α_e gradient in the equal-mass mergers and also of the accretion of a lower- α_e galaxy in the unequal-mass mergers. The final value of α_e depends more on the mass ratio than on the orbital angular momentum of the encounter. The lowest values of α_e are obtained in the $\xi_\star = 0.5$ major merger, while the remnants of the $\xi_\star = 0.2$ minor mergers have α_e intermediate between the $\xi_\star = 1$ and the $\xi_\star = 0.5$ major mergers. The effect on σ_e is variegated, ranging from equal-mass mergers that make σ_e increase to minor mergers that make σ_e decrease. With the only exception of the head-on $\xi_\star = 0.2$ merger (arrow pointing towards the smallest square in Fig. 7), for which the remnant lies on the same $\alpha_e\text{-}\sigma_e$ power law followed by the progenitor galaxies, the effect of the dry merging is to move the galaxies away from the $\alpha_e\text{-}\sigma_e$ relation, producing remnants with low α_e for their σ_e (compared to the progenitor galaxies). The error bars in Fig. 7 give a measure of the projection effects in σ_e , due to the fact that the remnants are not spherically symmetric (the projection effects on α_e turn out to be negligible). We note that these projection effects are well within the intrinsic scatter of the observed correlation, which is ≈ 0.1 dex in α_e at given σ_e (see Section 1) and thus, given the slope of the relation (equation 2), ≈ 0.3 dex in σ_e at given α_e .

In order to compare quantitatively the effect on σ_e and α_e of mergers with different ξ_\star , it is useful to introduce the quantities

$$\gamma_\sigma \equiv \frac{\log \sigma_{e,\text{remn}} - \log \sigma_{e,\text{main}}}{\log M_{\star,\text{remn}} - \log M_{\star,\text{main}}} = \frac{\log \tilde{\sigma}_{e,\text{remn}}}{\log(1 + \xi_\star)} \quad (21)$$

and

$$\gamma_\alpha \equiv \frac{\log \alpha_{e,\text{remn}} - \log \alpha_{e,\text{main}}}{\log M_{\star,\text{remn}} - \log M_{\star,\text{main}}} = \frac{\log \tilde{\alpha}_{e,\text{remn}}}{\log(1 + \xi_\star)}, \quad (22)$$

which measure the variations of, respectively, $\log \sigma_e$ and $\log \alpha_e$ per unit logarithmic stellar mass increase (the values of $\tilde{\sigma}_{e,\text{remn}}$ and $\tilde{\alpha}_{e,\text{remn}}$ are given for each simulation in Table 1; we have used $M_{\star,\text{remn}}/M_{\star,\text{main}} = 1 + \xi_\star$, because the stellar mass loss turns out to be negligible in the considered mergers). In our set-D simulations we find $-0.48 \lesssim \gamma_\sigma \lesssim 0.11$ and $-0.16 \lesssim \gamma_\alpha \lesssim -0.03$, where the lowest values are for $\xi_\star = 0.2$ and the highest for $\xi_\star = 1$.

For a more direct comparison with observational data, we plot in Fig. 8 a $\sigma_e\alpha_e$ diagram in which the remnants are assumed to lie on the observed present-day $\alpha_e\text{-}\sigma_e$ relation (solid line). Note that, different from Fig. 7, in Fig. 8 we normalize α_e to $\alpha_{e,\text{remn}}$ and σ_e to $\sigma_{e,\text{remn}}$, so, by construction, all the remnants are at the same point, which is assumed to lie on the observed present-day $\alpha_e\text{-}\sigma_e$ relation. In Fig. 8 the circles and squares indicate the positions of the main galaxies of the simulations, assuming for $\sigma_{e,\text{remn}}$ and $\alpha_{e,\text{remn}}$ the mean values measured over all the considered projections of the corresponding remnants, and the error bars, as in Fig. 7, give a measure of the projection effects due to deviations from spherical symmetry. In Fig. 8 the squares and the circles can be considered the progenitors of present-day ETGs that lie on the observed $\alpha_e\text{-}\sigma_e$ relation. All the progenitors, but that of the head-on $\xi_\star = 0.2$ merger, lie above the $\alpha_e\text{-}\sigma_e$ relation.

4.5 Merger-driven evolution of the $\alpha_e\text{-}\sigma_e$ relation

We recall that so far we have not considered the effects of full merging hierarchies, but only the effects of single binary mergers. Here we attempt to predict the cosmological evolution of the $\alpha_e\text{-}\sigma_e$ relation based on the results of our simulations.

4.5.1 Purely dry merging hierarchies

When cosmologically motivated merging hierarchies are considered, massive galaxies in the redshift range $0 \lesssim z \lesssim 2$ experience merging histories with average mass-weighted merger stellar mass ratio $\langle \xi \rangle_\star$ in the range $0.3 \lesssim \langle \xi \rangle_\star \lesssim 0.5$ (Sonnenfeld et al. 2017). We thus expect that in a cosmologically motivated merging history a massive ETG moves in the $\sigma_e\alpha_e$ plane along a direction which is in between those of the $\xi_\star = 0.2$ and $\xi_\star = 0.5$ simulations (arrows starting from small and intermediate circles and squares in Fig. 8).

Given that in our model the satellite and main galaxies lie on a $\alpha_e\text{-}\sigma_e$ power law with the same slope as that observed at $z \approx 0$, our results suggest a possible scenario in which the $\alpha_e\text{-}\sigma_e$ relation evolves by maintaining its slope and changing its normalisation: at given σ_e , α_e is higher at higher redshift. Such a scenario is qualitatively represented in Fig. 9. While α_e invariably decreases in this model, the evolution of σ_e is more uncertain: even limiting to simulations with $\xi_\star = 0.2$ and $\xi_\star = 0.5$, bracketing the cosmologically motivated value of $\langle \xi \rangle_\star$, σ_e decreases in some cases and increases in others.

Let us consider an individual galaxy that experiences a merging hierarchy that produces an increase in stellar mass $\Delta \log M_\star$: the corresponding variations in σ_e and α_e , are given by $\Delta \log \sigma_e = \Delta \log M_\star \langle \gamma_\sigma \rangle$ and $\Delta \log \alpha_e = \Delta \log M_\star \langle \gamma_\alpha \rangle$, where $\langle \dots \rangle$ indicates the average over the merging history. Given the expected values of $\langle \xi \rangle_\star$, we can build a toy model by estimating these averages as the mean values obtained for our four set-D simulations with either $\xi_\star = 0.5$ or $\xi_\star = 0.2$: $\langle \gamma_\sigma \rangle = -0.135$ and $\langle \gamma_\alpha \rangle = -0.123$. The thick yellow arrows in Fig. 9 indicate the effect of these variations for individual galaxies increasing their stellar masses by a factor of three as a consequence of dry mergers and ending up onto the mean observed $\alpha_e\text{-}\sigma_e$ relation at $z \approx 0$. Given that a factor of three increase in stellar mass is expected from $z \approx 2$ to $z \approx 0$ (e.g. Sonnenfeld et al. 2017), we can interpret the starting points of the arrows as $z \approx 2$. In the hypothesis that ETGs over the entire σ_e range have experienced similar accretion histories, the net effect of the evolution of individual galaxies is that at higher redshift the $\alpha_e\text{-}\sigma_e$ had similar slope but higher normalisation (at given σ_e , α_e is predicted to be higher at higher z ; solid and dashed thick lines in Fig. 9). We note that, though the variation in stellar mass is as high as a factor of three, the predicted variation in the normalisation of the $\alpha_e\text{-}\sigma_e$ relation is just 0.04 dex, much smaller than the intrinsic scatter of the present-day relation (0.12 dex; thin dotted lines in Fig. 9).

We recall that in our simulations the satellite and main galaxies are assumed to follow $R_e\text{-}M_\star$ and $\sigma_e\text{-}M_\star$ relations with slopes similar to those observed for massive ETGs (Section 2.2): in this sense the satellites can be considered *compact*, following the terminology of Hilz et al. (2013). This choice is consistent with the fact that in the present-day Universe the $R_e\text{-}M_\star$ and $\sigma_e\text{-}M_\star$ relations are found to be similar for central and satellite galaxies (Spindler & Wake 2017; Wang et al. 2020). However, the properties of satellite galaxies at higher z are poorly constrained, so it is not excluded that the accreted satellites can be *diffuse*, i.e. having lower σ_e and larger R_e for their stellar mass (Hilz et al. 2013).

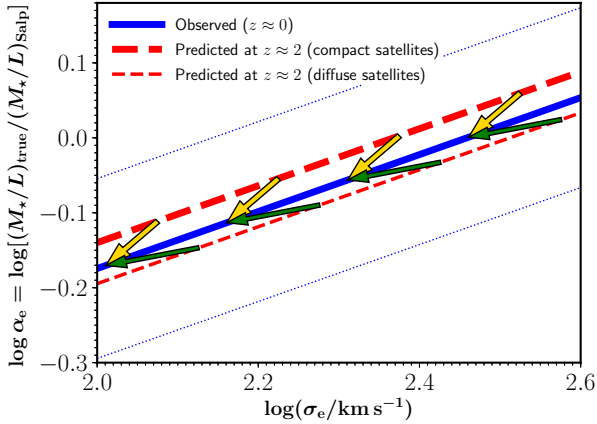


Figure 9. Toy model, based on the results of the N -body simulations presented in this work, representing the dry-merger driven evolution of the α_e - σ_e relation of ETGs. Here σ_e is expressed in physical units and α_e is defined as $(M_*/L)_{\text{true}}/(M_*/L)_{\text{Salp}}$, thus taking the Salpeter IMF as reference. The solid line represents the best fit found by Posacki et al. (2015) for present-day ETGs (equation 2) and the dotted lines indicate the intrinsic scatter of the observed correlation. The thick arrows indicate the evolution of individual galaxies expected from $z \approx 2$ progenitors to $z \approx 0$ descendants (assuming that, on average, the stellar mass of individual galaxies has grown by a factor of three), when the accreted satellites are compact, such as those considered in our simulations. The thick dashed line represents the correlation predicted in this case at $z \approx 2$. The thin arrows indicate qualitatively how the corresponding thick arrows are modified if the accreted satellites are so diffuse to lead to an opposite evolution of the correlation (thin dashed line).

The assumption of compact satellites might be observationally motivated by the fact that there is no evidence of evolution of the slopes of the R_e - M_* and σ_e - M_* relations (van der Wel et al. 2014; Cannarozzo et al. 2020), though a steepening of the σ_e - M_* relation with increasing redshift is not excluded (Cannarozzo et al. 2020), which might instead favour the hypothesis of diffuse satellites.

Dissipationless mergers with diffuse satellites have been studied with N -body simulations by Hilz et al. (2013). Based on the results of Hilz et al.’s simulations and on well-known properties of interacting stellar systems, it is easy to predict qualitatively how the dry-merger driven evolution of galaxies in the σ_e - α_e plane changes if the accreted satellites are diffuse. A diffuse satellite, being loosely bound, is easily disrupted during the merger and deposits most of its stars in the outskirts of the main galaxy, thus producing a remnant with central α_{IMF} similar to the progenitor and lower α_{IMF} in the outskirts (thus steepening the original α_{IMF} gradient). As a consequence, α_e of the remnant will be only slightly lower than that of the main progenitor. Because of the accretion of loosely bound stars, the velocity dispersion of the remnant is lower than in the case of compact satellites (Naab et al. 2009), so σ_e decreases more when the satellites are diffuse. Qualitatively, the net effect is that dry mergers with diffuse satellites, compared to those with compact satellites, move galaxies more horizontally in the σ_e - α_e plane (thin green arrows in Fig. 9), possibly leading to a different evolution of the α_e - σ_e relation, with lower α_e at higher z , at given σ_e (thin dashed line in 9).

4.5.2 The effect of dissipation and star formation

The simulations used in this work are admittedly idealized, not only because they are not within a fully cosmological context, but also because they are completely dissipationless. Present-day ETGs are poor in cold gas and have a stellar component that is dominated by old stellar populations, so if they experienced mergers in relatively recent times, these mergers must have been essentially dry. Detailed analyses of the stellar population properties of ETGs indicate that at most a few per cent of their stellar mass formed at $z \lesssim 1$ (e.g. Trager et al. 2000, Thomas et al. 2010; see also Sonnenfeld et al. 2014 and references therein). Though this fraction is small, such star formation could affect non-negligibly the evolution of both σ_e and α_e if, as expected, it occurs in the central regions of the galaxies. Moreover, star formation might have contributed more at $z \gtrsim 1$.

Compared to purely dry mergers, slightly ‘wet’ mergers, i.e. with some dissipation and star formation, are expected to produce remnants more compact and thus with higher stellar velocity dispersion (Robertson et al. 2006; Ciotti et al. 2007; Sonnenfeld et al. 2014). The effect of dissipation and star formation on α_e depends on the IMF of the stars that are formed in the star formation episodes occurring during the mergers, which is of course highly uncertain. Based on the proposal that the IMF is heavier when the pressure of the star-forming gas is higher (e.g. Barber et al. 2018 and references therein), one might expect that at lower z stars form with IMF lighter than that of stars formed at higher redshift (because the pressure of the gas from which stars form tends to decrease with cosmic time; Barber et al. 2019b). However, as far as we know, it is not excluded, either theoretically or observationally, that at lower z stars can form with heavier IMF.

4.5.3 Comparison with observations and with previous models

The theoretical predictions on the evolution of the α_e - σ_e relation can be tested with measurements of α_e and σ_e at different redshifts. However, so far such measurements are relatively rare and it is difficult to draw robust conclusions. On the one hand, Sonnenfeld et al. (2015) find that in an observed sample of lens ETGs, α_e tends to decrease with increasing redshift, at fixed σ_e , out to $z \approx 0.8$. On the other hand, Martín-Navarro et al. (2015b) find that massive ETGs at $z \approx 1$ have IMF similar to (or slightly heavier than) present-day ETGs with comparable stellar velocity dispersion. Also Shetty & Cappellari (2014) find that massive ETGs at $z \approx 0.75$ have, at given σ_e , IMF similar to that of lower- z galaxies (or slightly heavier; see Sonnenfeld et al. 2017). Recently, Mendel et al. (2020) measured α_e and σ_e for a sample of quiescent galaxies at $1.4 < z < 2.1$, finding a steeper α_e - σ_e relation, which overlaps with the $z \approx 0$ relation at the high- σ_e end. The trend found by Sonnenfeld et al. (2015) and Mendel et al. (2020) (higher- z galaxies tend to have lower α_e at given σ_e) appears in tension with the compact-satellite evolutionary model depicted in Fig. 9 and more consistent with the hypothesis of diffuse satellites. It should be noted, though, that the measurements of both Sonnenfeld et al. (2015) and Mendel et al. (2020) are relying on a set of assumptions, most notably that of a spatially constant stellar mass-to-light ratio at all redshifts. This assumption can have a big impact on their estimates of the IMF (see e.g. Sonnenfeld et al. 2018 and Bernardi et al. 2018) and, consequently, on their measured trend with redshift.

The theoretical model of Sonnenfeld et al. (2017), who found a negligible evolution of the α_e - σ_e relation (i.e. α_e at given σ_e independent of redshift), lies in between the compact-satellite and the

diffuse-satellite scenarios depicted in Fig. 9. In our simulations both the effective velocity dispersion and the effective IMF mismatch parameter of the remnants are computed self-consistently accounting for the internal kinematics, structure and α_{IMF} distribution of the N -body systems. In their statistical approach, Sonnenfeld et al. (2017) assume that σ_e is proportional to the virial velocity dispersion and that α_e of the remnant is the weighted mean of α_e of the progenitor galaxies. When this weighted mean is adopted, α_e of the remnant is overestimated compared to the case of compact satellites, in which most of the variation of α_{IMF} occurs in the center, so, in this respect, the model of Sonnenfeld et al. (2017) is closer to the diffuse-satellite scenario. Qualitatively, our compact-satellite scenario predicts an evolution of the α_e - σ_e relation broadly consistent with the cosmological model ‘LoM’ of Barber et al. (2019b) and with that of Blancato et al. (2017), which both predict higher α_e at higher redshift, for given σ_e .

5 CONCLUSIONS

We have studied the effect of dissipationless (dry) mergers on the distribution of the IMF mismatch parameter α_{IMF} in ETGs using the results of dissipationless binary major and minor merging simulations. Our main conclusions are the following.

- Dissipationless mergers tend to make the α_{IMF} profiles of ETGs shallower, and in particular to produce flat central ($R \lesssim 0.3R_e$) α_{IMF} distributions.
- Dissipationless mergers do not alter significantly the shape of the spatially resolved distributions in the $\sigma_{\text{los}}\alpha_{\text{IMF}}$ space: when the progenitor galaxies have realistic distributions in this space, this is true also for the merger remnants.
- Individual galaxies undergoing dry mergers move, in the space of integrated quantities $\alpha_e\sigma_e$, by decreasing their α_e , due to the erosion of α_{IMF} gradients and mixing with stellar populations with lighter IMF, while their σ_e can either decrease or increase, depending on the merging orbital parameters and mass ratio. σ_e tends to decrease in cosmologically motivated merging histories.
- The dry-merger driven evolution of the α_e - σ_e relation of ETGs depends on the nature of the accreted satellites: galaxies of given σ_e are expected to have higher α_e at higher redshift if the satellites are compact, but the trend can be opposite if the satellites are sufficiently diffuse.

The effects of dry mergers on the α_{IMF} distribution and on the α_e - σ_e predicted by our model are not dramatic and are thus broadly consistent with the currently available observational constraints, which are however limited and somewhat controversial. Some observational estimates of the evolution of the α_e - σ_e relation of ETGs (Sonnenfeld et al. 2015; Mendel et al. 2020) indicate that α_e at given σ_e tends to be lower than at higher z . This is in tension with the predictions of dry-merger simulations in which the satellites are compact, and suggest that accretion of diffuse satellites might be invoked to reconcile a dry-merging driven evolution with observational data. Additional measurements of the properties of the IMF of ETGs beyond the present-day Universe are necessary to further test the two-phase formation model of massive ETGs, in which essentially dissipationless mergers have an important role at $z \lesssim 2$. A very promising possibility is to estimate α_e of lens ETGs by combining constraints on the total mass from gravitational lensing with spatially resolved kinematics (see Treu et al. 2010), which will be feasible over a significant redshift range with forthcoming telescopes and instruments (e.g. Shajib et al. 2018).

DATA AVAILABILITY

The data underlying this article will be shared on reasonable request to the corresponding author.

ACKNOWLEDGEMENTS

FC acknowledges support from grant PRIN MIUR 20173ML3WW_001.

References

- Alton P. D., Smith R. J., Lucey J. R., 2017, *MNRAS*, **468**, 1594
 Alton P. D., Smith R. J., Lucey J. R., 2018, *MNRAS*, **478**, 4464
 Barber C., Crain R. A., Schaye J., 2018, *MNRAS*, **479**, 5448
 Barber C., Schaye J., Crain R. A., 2019a, *MNRAS*, **482**, 2515
 Barber C., Schaye J., Crain R. A., 2019b, *MNRAS*, **483**, 985
 Bastian N., Covey K. R., Meyer M. R., 2010, *ARA&A*, **48**, 339
 Bernardi M., Sheth R. K., Domínguez Sanchez H., Fischer J. L., Chae K. H., Huertas-Company M., Shankar F., 2018, *MNRAS*, **477**, 2560
 Blancato K., Genel S., Bryan G., 2017, *ApJ*, **845**, 136
 Boylan-Kolchin M., Ma C.-P., Quataert E., 2006, *MNRAS*, **369**, 1081
 Calura F., Menci N., 2009, *MNRAS*, **400**, 1347
 Cannarozzo C., Sonnenfeld A., Nipoti C., 2020, *MNRAS*, in press, p. arXiv:1910.06987
 Cappellari M., et al., 2012, *Nature*, **484**, 485
 Chabrier G., 2003, *PASP*, **115**, 763
 Chattopadhyay T., De T., Warlu B., Chattopadhyay A. K., 2015, *ApJ*, **808**, 24
 Cimatti A., Nipoti C., Cassata P., 2012, *MNRAS*, **422**, L62
 Cimatti A., Fraternali F., Nipoti C., 2019, Introduction to galaxy formation and evolution: from primordial gas to present-day galaxies. Cambridge University Press
 Ciotti L., Stiavelli M., Braccetti A., 1995, *MNRAS*, **276**, 961
 Ciotti L., Lanzoni B., Volonteri M., 2007, *ApJ*, **658**, 65
 Collier W. P., Smith R. J., Lucey J. R., 2018, *MNRAS*, **473**, 1103
 Conroy C., van Dokkum P. G., 2012, *ApJ*, **760**, 71
 Davis T. A., McDermid R. M., 2017, *MNRAS*, **464**, 453
 Dehnen W., 1993, *MNRAS*, **265**, 250
 Domínguez Sánchez H., Bernardi M., Brownstein J. R., Drory N., Sheth R. K., 2019, *MNRAS*, **489**, 5612
 Domínguez Sánchez H., Bernardi M., Nikakhtar F., Margalef-Bentabol B., Sheth R. K., 2020, *MNRAS*, **495**, 2894
 Dutton A. A., Mendel J. T., Simard L., 2012, *MNRAS*, **422**, 33
 Falcón-Barroso J., et al., 2017, *A&A*, **597**, A48
 Fontanot F., De Lucia G., Hirschmann M., Bruzual G., Charlot S., Zibetti S., 2017, *MNRAS*, **464**, 3812
 Gargiulo I. D., et al., 2015, *MNRAS*, **446**, 3820
 Hilz M., Naab T., Ostriker J. P., 2013, *MNRAS*, **429**, 2924
 Hopkins A. M., 2018, *Publ. Astron. Soc. Australia*, **35**, e039
 Kroupa P., 2001, *MNRAS*, **322**, 231
 La Barbera F., et al., 2019, *MNRAS*, **489**, 4090
 Li H., et al., 2017, *ApJ*, **838**, 77
 Londrillo P., Nipoti C., Ciotti L., 2003, *Memorie della Societa Astronomica Italiana Supplementi*, **1**, 18
 Martín-Navarro I., La Barbera F., Vazdekis A., Falcón-Barroso J., Ferreras I., 2015a, *MNRAS*, **447**, 1033
 Martín-Navarro I., et al., 2015b, *ApJ*, **798**, L4
 Mendel J. T., et al., 2020, *ApJ*, **899**, 87
 Merritt D., 1985, *AJ*, **90**, 1027
 Naab T., Johansson P. H., Ostriker J. P., 2009, *ApJ*, **699**, L178
 Nagashima M., Lacey C. G., Okamoto T., Baugh C. M., Frenk C. S., Cole S., 2005, *MNRAS*, **363**, L31
 Navarro J. F., Frenk C. S., White S. D. M., 1996, *ApJ*, **462**, 563
 Nipoti C., Londrillo P., Ciotti L., 2003a, *MNRAS*, **342**, 501

- Nipoti C., Stiavelli M., Ciotti L., Treu T., Rosati P., 2003b, *MNRAS*, **344**, 748
- Nipoti C., Londrillo P., Ciotti L., 2006, *MNRAS*, **370**, 681
- Nipoti C., Treu T., Bolton A. S., 2009, *ApJ*, **703**, 1531
- Nipoti C., Treu T., Leauthaud A., Bundy K., Newman A. B., Auger M. W., 2012, *MNRAS*, **422**, 1714
- Oldham L., Auger M., 2018, *MNRAS*, **474**, 4169
- Oser L., Ostriker J. P., Naab T., Johansson P. H., Burkert A., 2010, *ApJ*, **725**, 2312
- Osipkov L. P., 1979, *Soviet Astronomy Letters*, **5**, 42
- Parikh T., et al., 2018, *MNRAS*, **477**, 3954
- Posacki S., Cappellari M., Treu T., Pellegrini S., Ciotti L., 2015, *MNRAS*, **446**, 493
- Raskutti S., Greene J. E., Murphy J. D., 2014, *ApJ*, **786**, 23
- Robertson B., Cox T. J., Hernquist L., Franx M., Hopkins P. F., Martini P., Springel V., 2006, *ApJ*, **641**, 21
- Rosani G., Pasquali A., La Barbera F., Ferreras I., Vazdekis A., 2018, *MNRAS*, **476**, 5233
- Salpeter E. E., 1955, *ApJ*, **121**, 161
- Shajib A. J., Treu T., Agnello A., 2018, *MNRAS*, **473**, 210
- Shetty S., Cappellari M., 2014, *ApJ*, **786**, L10
- Smith R. W., 2020, *ARA&A*, in press
- Smith R. J., Lucey J. R., Conroy C., 2015, *MNRAS*, **449**, 3441
- Sonnenfeld A., Nipoti C., Treu T., 2014, *ApJ*, **786**, 89
- Sonnenfeld A., Treu T., Marshall P. J., Suyu S. H., Gavazzi R., Auger M. W., Nipoti C., 2015, *ApJ*, **800**, 94
- Sonnenfeld A., Nipoti C., Treu T., 2017, *MNRAS*, **465**, 2397
- Sonnenfeld A., Leauthaud A., Auger M. W., Gavazzi R., Treu T., More S., Komiyama Y., 2018, *MNRAS*, **481**, 164
- Sonnenfeld A., Jaelani A. T., Chan J., More A., Suyu S. H., Wong K. C., Oguri M., Lee C.-H., 2019, *A&A*, **630**, A71
- Spindler A., Wake D., 2017, *MNRAS*, **468**, 333
- Spiniello C., Trager S., Koopmans L. V. E., Conroy C., 2014, *MNRAS*, **438**, 1483
- Thomas D., Maraston C., Schawinski K., Sarzi M., Silk J., 2010, *MNRAS*, **404**, 1775
- Tortora C., Romanowsky A. J., Napolitano N. R., 2013, *ApJ*, **765**, 8
- Trager S. C., Faber S. M., Worthey G., González J. J., 2000, *AJ*, **120**, 165
- Tremaine S., Richstone D. O., Byun Y.-I., Dressler A., Faber S. M., Grillmair C., Kormendy J., Lauer T. R., 1994, *AJ*, **107**, 634
- Treu T., Auger M. W., Koopmans L. V. E., Gavazzi R., Marshall P. J., Bolton A. S., 2010, *ApJ*, **709**, 1195
- Vaughan S. P., Davies R. L., Zieleniewski S., Houghton R. C. W., 2018, *MNRAS*, **475**, 1073
- Veale M., Ma C.-P., Greene J. E., Thomas J., Blakeslee J. P., Walsh J. L., Ito J., 2018, *MNRAS*, **473**, 5446
- Vogelsberger M., et al., 2014, *MNRAS*, **444**, 1518
- Wang E., Wang H., Mo H., van den Bosch F. C., Yang X., 2020, *ApJ*, **889**, 37
- Wechsler R. H., Tinker J. L., 2018, *ARA&A*, **56**, 435
- Wetzel A. R., 2011, *MNRAS*, **412**, 49
- White S. D. M., 1980, *MNRAS*, **191**, 1P
- Zieleniewski S., Houghton R. C. W., Thatte N., Davies R. L., Vaughan S. P., 2017, *MNRAS*, **465**, 192
- de Zeeuw P. T., et al., 2002, *MNRAS*, **329**, 513
- van Dokkum P., Conroy C., Villaume A., Brodie J., Romanowsky A. J., 2017, *ApJ*, **841**, 68
- van der Wel A., et al., 2014, *ApJ*, **788**, 28

APPENDIX A: VARYING THE α_{IMF} PROFILES OF THE PROGENITOR GALAXIES

In Section 4 we have described how we assign α_{IMF} to the stellar particles of the simulation by choosing the values of the dimensionless parameters A_{IMF} , B_{IMF} and C_{IMF} . Here we illustrate the effect of changing the values of these parameters. We focus on equal-mass

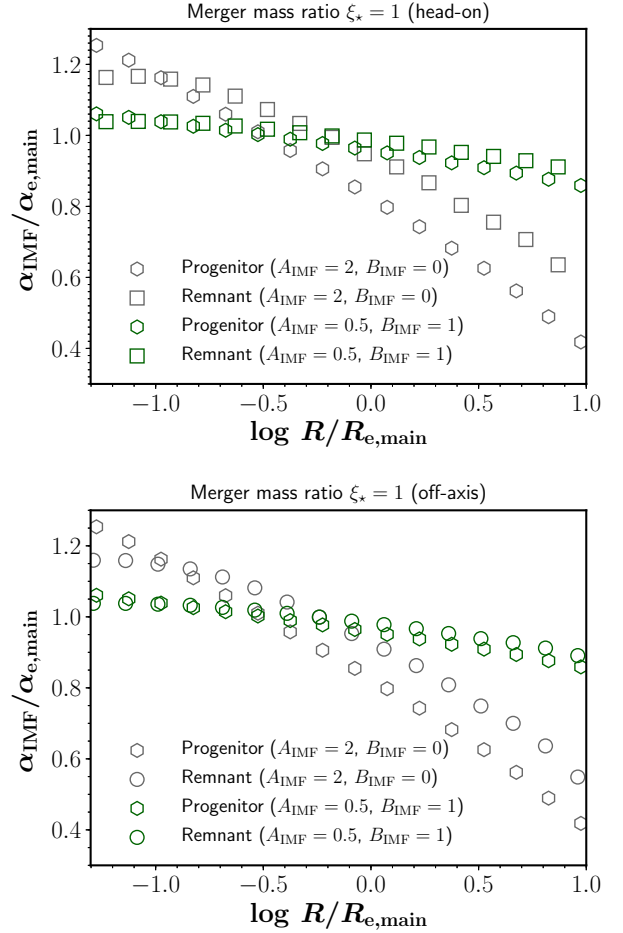


Figure A1. Same as lower panel of Fig. 1, but for the equal-mass head-on merger models D1h and D1h_bis (upper panel), and off-axis merger models D1o and D1o_bis (lower panel). Models D1h_bis and D1o_bis are based on the same simulations as models D1h and D1o, respectively, but in post-processing different values of A_{IMF} and B_{IMF} are assumed. The progenitor galaxies (hexagons) and the remnants (squares and circles) of models D1h and D1o ($A_{\text{IMF}} = 2$, $B_{\text{IMF}} = 0$) are represented by grey symbols, while those of models D1h_bis and D1o_bis ($A_{\text{IMF}} = 0.5$, $B_{\text{IMF}} = 1$) by green symbols.

mergers simulations and we fix in all cases $C_{\text{IMF}} = 1$ so that the two progenitor galaxies are identical, not only structurally and kinematically, but also in terms of distribution of α_{IMF} . In particular, we describe here the properties of models D1h_bis and D1o_bis, comparing them with those of models D1h and D1o. Models D1h_bis and D1o_bis are based on the same simulations as models D1h and D1o, respectively, but in post-processing different values of A_{IMF} and B_{IMF} are assumed (see Table 1). The progenitor galaxies of models D1h_bis and D1o_bis have weaker dependence of α_{IMF} on the integral of motion Q ($A_{\text{IMF}} = 0.5$ and $B_{\text{IMF}} = 1$) and thus shallower gradients of α_{IMF} (Fig. A1) than those of models D1h and D1o, which have $A_{\text{IMF}} = 2$ and $B_{\text{IMF}} = 0$. In this sense, models D1h_bis and D1o_bis are less realistic than models D1h and D1o, when compared to the α_{IMF} gradients inferred for observed ETGs (see Section 4.2). Due to the shallow α_{IMF} profiles of their progenitor galaxies, the remnants of models D1h_bis and D1o_bis have normalized α_{IMF} profiles almost indistinguishable from those of the progenitors (Fig. A1). Fig. A2 shows that both the progen-

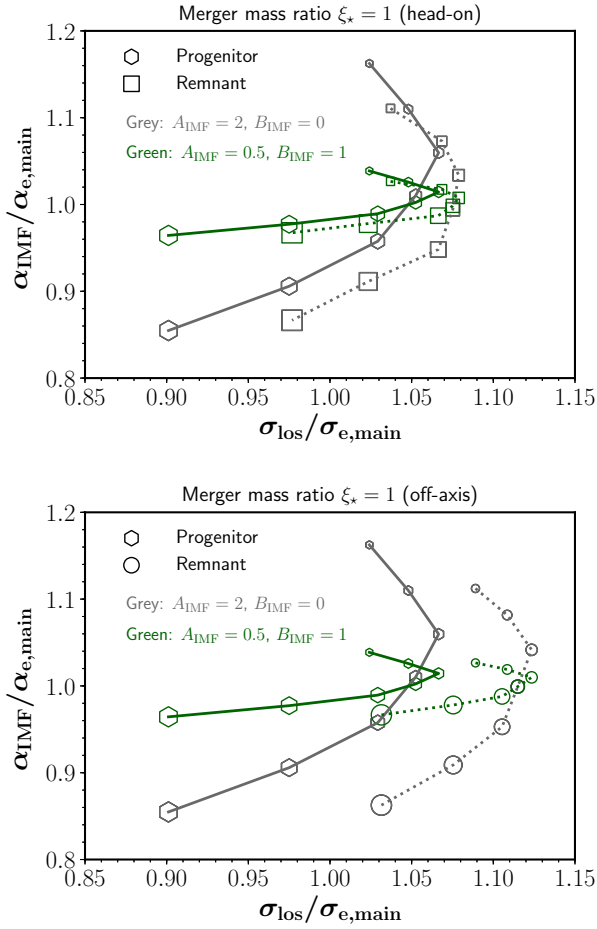


Figure A2. Same as top panel of Fig. 6, but for the equal-mass head-on merger models D1h and D1h_bis (upper panel), and off-axis merger models D1o and D1o_bis (lower panel). Symbols and colours are the same as in Fig. A1.

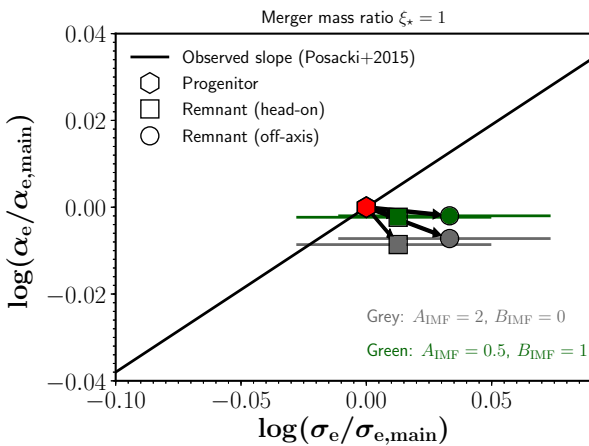


Figure A3. Same as Fig. 7, but for progenitor galaxy (hexagon) and the remnants of the equal-mass merger models D1h (grey square), D1o (grey circle), D1h_bis (green square) and D1o_bis (green circle).

itors and the remnants of models D1h_bis and D1o_bis have distributions significantly different from the progenitors and the remnants of models D1h and D1o. For given A_{IMF} and B_{IMF} , the distributions in the $\sigma_{\text{los}}\alpha_{\text{IMF}}$ space of the remnants and the progenitors differ essentially only for variations in σ_{los} . Consistently, also the merger-driven evolution in the $\sigma_e\alpha_e$ space is weaker for models D1h_bis and D1o_bis than for models D1h and D1o (Fig. A3). Models D1h_bis and D1o_bis are presented here only for the purpose of illustrating the effect of changing the values of A_{IMF} and B_{IMF} , but, for the aforementioned reasons, should not be considered as representative of real ETGs as models D1h and D1o.

APPENDIX B: MERGERS BETWEEN NON-HOMOLOGOUS GALAXIES

In Section 4, we have presented results of simulations (set D) in which the main and satellite galaxies are homologous stellar systems. Of course, this simplification is not fully justified, especially in the case of minor mergers, because we expect that galaxies of different stellar mass differ in their structural properties, for instance in the distribution and amount of dark matter, relative to the baryonic matter (Wechsler & Tinker 2018). Here we consider $\xi_* = 0.2$ simulations of sets D3 (0.2D3h and 0.2D3o) and D4 (0.2D4h and 0.2D4o), in which the structure of the satellite progenitor galaxy differs significantly from that of the main galaxy, and we compare them with the corresponding simulations of set D (0.2Dh and 0.2Do). The values of the parameters of these sets of simulations is reported in Table 1 and are chosen to span the range of values expected for real galaxies, with dark-to-luminous mass ratios ranging from 35 to 70 (see Sonnenfeld et al. 2014). Due to the non-homology, also the σ_{los} profiles of the satellite progenitor galaxies are not identical in simulations of sets D, D3 and D4, but the σ_{los} profiles of the remnants are almost indistinguishable out to $\approx 3R_e$. The values of C_{IMF} are such that the satellite and main galaxies lie on the same α_e - σ_e power-law relation (equation 2), and are thus different for the three sets of $\xi_* = 0.2$ simulations, but the α_{IMF} profiles of the remnants are similar in the three cases. Here we show only the distributions of α_{IMF} as a function of σ_{los} (Fig. B1), which for the remnants of simulations of sets D3 and D4 are very similar to those of the corresponding simulations of set D. We thus conclude that our results do not depend significantly on the amount and distribution of dark-matter in the satellite galaxy.

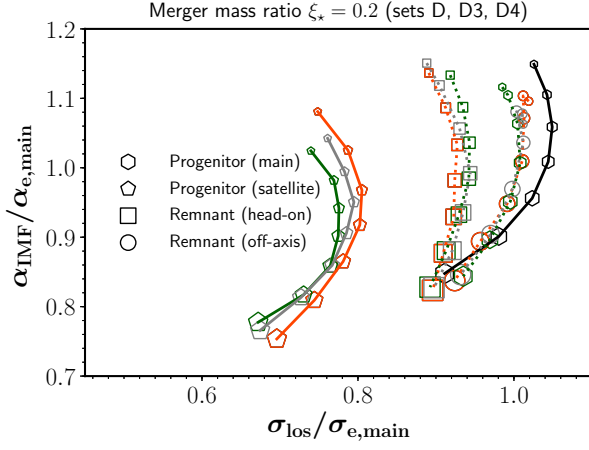


Figure B1. Same as bottom panel of Fig. 6, but for the $\xi_* = 0.2$ head-on merger simulations 0.2Dh (set D; grey), 0.2D3h (set D3; red) and 0.2D4h (set D4; green), and off-axis merger simulations 0.2Do (set D; grey), 0.2D3o (set D3; red) and 0.2D4o (set D4; green).